Mach cone shocks in a two-dimensional Yukawa solid using a complex plasma

D. Samsonov* and J. Goree[†]

Department of Physics and Astronomy, The University of Iowa, Iowa City, Iowa 52242

H. M. Thomas and G. E. Morfill

Max-Planck-Institut für Extraterrestrische Physik, Giessenbachstrasse, 85740 Garching, Germany

(Received 12 November 1999)

Mach cones were studied experimentally in a two-dimensional Yukawa solid consisting of charged micrometer particles suspended as a layer in a plasma. These cones were V-shaped shocks produced spontaneously by a supersonic particle moving below the main two-dimensional particle layer. The cones had a double structure. The first cone was compressional and particles moved forward, and it was followed by a second cone, which was rarefactional, where particles moved backward. Over the limited range of speed V attained by the supersonic particles in this experiment, the angle μ of the cone was found to obey the Mach cone rule $\sin \mu = c/V$, where c is the medium's sound speed. The cones caused only elastic deformations in the crystal lattice, except in a narrow track behind the cone's vertex. The wings of the cones can be analyzed as linear shocks in two dimensions. Using spatially resolved measurements of the particle number density and velocity and applying the Hugoniot relations for shocks in two dimensions, we found that the pressure inside the first Mach cone was greater than in the undisturbed medium by a factor of 1.3–1.6. The cone angle was also used to measure the charge in this experiment.

PACS number(s): 82.70.Dd, 52.25.Vy, 83.50.Tq, 52.35.Tc

I. INTRODUCTION

Mach cones are V-shaped disturbances or shock waves produced by a supersonic object moving through a medium. While they are best known in gas dynamics, they also occur in solid matter. Here we take an interdisciplinary approach to demonstrate that Mach cones exist in complex fluids.

The complex fluid we use is a suspension of charged microsphere particles in an ionized gas. This system has been termed a complex plasma in analogy to a complex fluid. It is similar to to a colloidal suspension, but with a greatly reduced damping rate, due to the use of a rarefied gas rather than a liquid as the suspension medium. The particles are charged by collecting electrons and ions from the ionized gas. Having no buoyancy, the particles must be electrostatically levitated above a negatively charged horizontal electrode. Through their interparticle repulsion and the external confinement provided by the electric fields in the plasma, the particles arrange themselves in an ordered lattice.

This system serves as a macroscopic model system for solid atomic matter. The arrangement of the microspheres in a lattice is analogous to atoms in a real crystal. The advantage of a model system is that it allows direct *in-situ* measurement of the positions and velocities of all the particles in the system, which is not possible in an atomic solid. Thus, we can observe and measure the microscopic dynamics of phenomena, such as shocks and Mach cones.

Because Mach cones are a kind of shock wave, we present our work as a study not only of Mach cones in solids, but also as a study of shocks in solids. Most experiments with shocks in solids use atomic matter [1]. Our experiment allows us to make *in situ* and time-resolved microscopic measurements of the structure of the solid, showing how it develops during the shock process.

The underlying physics of Mach cones and shocks is essentially the same in two-dimensional systems as in three dimensions. In this paper we report experiments carried out in a two-dimensional suspension of particles.

In addition to being a model system for atomic matter, complex plasmas are also interesting in their own right, as a form of matter that occurs naturally. Astronomers, in fact, were the first to study complex plasmas extensively. They use the term ''dusty plasma,'' which has also been adopted widely by researchers in other fields. For example, Saturn's rings consist not only of boulders, but also dust particles immersed in the Saturnian magnetospheric plasma [2,3].

The experiments we report here employ the methods and instrumentation that we introduced in our first paper on Mach cones [4]. In this paper we develop additional analysis methods and we present further results. We have written this paper with the intention that it should be accessible to readers with diverse scientific backgrounds.

II. BACKGROUND INFORMATION

A. Mach cones

A supersonic object moving in a compressible medium creates a pressure disturbance that is not felt upstream from the object. The cone that confines the disturbance is called a Mach cone. The front of the disturbance is often discontinuous and called a shock wave. Mach cones are well known in gas dynamics [5]. They are produced, for example, by bullets and supersonic jet planes. If the perturbing object moves

*Present address: Max-Planck-Institut für Extraterrestrische Physik, Garching, D-85740, Germany. Electronic address: dima@mpe.mpg.de

[†]Author to whom correspondence should be addressed. Electronic address: john-goree@uiowa.edu
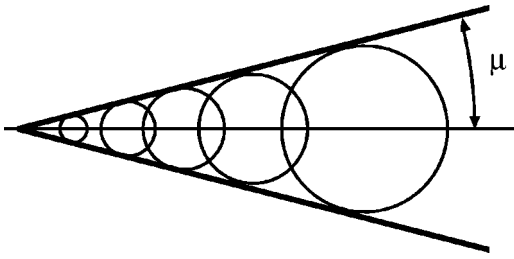
FIG. 1. Sketch of a Mach cone produced by a supersonic disturbance moving to the left. The cones are a superposition of spherical (or circular in 2D) waves generated by the moving disturbance. The semivertex angle μ is defined as the angle between the cone axis and the wave front.

straight at a constant velocity V, it creates expanding waves that are spherical in three dimensions, and circular in two dimensions. The superposition of these waves forms a cone, as sketched in Fig. 1. The Mach angle μ, defined as the semivertex angle of the cone, is determined by the geometry as

$$\mu = \sin^{-1}(1/M), \quad (1)$$

where $M = V/c$ is the Mach number of the supersonic object and c is the sound speed (acoustic speed) in the undisturbed medium.

Mach cones are also known to occur in solid matter. Cheng *et al.* [6] observed formation of the Mach cones in an elastic medium surrounding a fluid-filled borehole. They induced a surface wave propagating along the fluid-solid boundary of the borehole, and this excited P and S waves propagating into the bulk solid. The latter waves formed Mach cones. The wavefront of the surface wave acted as the supersonic object since its velocity was higher than that of the P and S waves.

Simulations have also predicted that a wake potential, similar to a Mach cone, is generated when a beam of energetic ions is fired into the surface of a solid [7–9]. Experiments of the type we describe here might be useful for understanding the contribution of the valence potential to the stopping power of ions in solid matter.

Ship waves have an appearance similar to Mach cones, but they are fundamentally different. A moving pointike disturbance generates either gravity or capillary waves on the fluid surface. These waves are transverse and strongly dispersive [10]. In contrast, in our experiments we found that the wave behind the disturbance was longitudinal and nondispersive, as discussed in Sec. VI.

B. Shock waves

Bond *et al.* [5] define a shock wave as a propagating disturbance characterized by an extremely rapid rise in pressure, temperature, and density. In general a shock wave cannot be treated as a small-amplitude linear wave. Under some circumstances shocks may cause the continuous motion of the gas or fluid without any periodic motion. Mathematically, shocks are treated as discontinuities with a thickness of a few mean free paths.

Shocks in gas dynamics are categorized according to the ratio of the gas pressure in front and behind the shock. When

this ratio is much bigger than unity, the shock is said to be strong, while it is said to be weak if the ratio is close to unity. In the limiting case when the pressure ratio is equal to unity, the shock wave becomes an acoustic wave [5].

Shocks in solids are widely studied in connection with explosions and impacts in the fields of material science and geophysics [1]. They consist of a rapid rise of pressure called a loading front, followed by an unloading wave. The unloading is a relaxation of the initial deformation, and it depends on the material properties.

Shocks in solids can be classified as elastic, elasticplastic, or strong according to the damage made to the medium [1]. The elastic shock regime is characterized by stress below the elastic limit, when the medium returns to its previous state. If the stress exceeds the elastic limit, the medium deforms plastically and this regime is called elasticplastic. In the strong shock regime the medium has almost fluid behavior.

Shocks in two-dimensional complex fluids have been studied previously using granular fluids [11]. This medium can behave like a solid, liquid, or gas [12]. A granular fluid is an example of a model system for studying atomic matter.

C. Model systems

The attraction of using macroscopic model systems to study phenomena such as phase transitions, waves, and shocks is that they allow experimental measurements that are often impractical in atomic solids and thin films. In particular, they often allow *in situ* measurements of particle position and velocity. These measurements can be made in real time. Moreover, because their interparticle interactions and bulk properties are analogous to those of atomic matter, model systems exhibit many of the same phenomena, without quantum effects.

Let us compare several different model systems. Colloids are formed by particles suspended as a two-dimensional (2D) layer or a three-dimensional (3D) volume in a liquid solution. The particles interact electrostatically *via* a repulsive Yukawa potential and can form crystals. As in other model systems, particles are measured optically, in some cases by direct imaging. One limitation of colloids as a model system is a high damping rate due to the friction forces exerted by the solvent fluid. It turns out that the waves in a colloidal crystal are almost always overdamped [13,14].

Complex plasmas are similar to colloidal suspensions, but they use a low-pressure ionized gas rather than a liquid solution as the background medium. Compared to colloids, they have a lower optical thickness, and a damping rate [15] that is lower by five orders of magnitude. The latter makes it possible to observe waves that are not overdamped. We will explain complex plasmas in greater detail below.

Granular materials are large conglomerations of discrete macroscopic particles. The particles interact *via* a repulsive hard sphere potential, in comparison to the soft sphere interaction of colloids and complex plasmas. This system can be in a solid-, liquid-, or gaslike state, and it can propagate waves [12]. Granular materials can display rather unusual behavior. Imaging is most practical with 2D granular materials [11] since bulk 3D systems are not translucent. Shocks in 2D granular materials were imaged in the experiment reported in Ref. [11],

Another model system is the bubble raft, which is a 2D layer of soap bubbles on a water surface. Bubbles interact with attraction-repulsion forces [16]. These have been used for modeling of the indentation hardness test of solid surfaces.

In our experiment, polymer microsphere particles were suspended as a horizontal monolayer. Thus the system is two dimensional. Because the particles were electrostatically charged, and they were immersed in a medium with free electrons and ions, they interacted *via* a screened Coulomb, i.e., Yukawa, potential. The lattice in our experiment was triangular with hexagonal symmetry.

D. Complex plasmas

Here we explain in greater detail complex plasmas, which are the model system used in this paper. We have attempted here to explain this topic so that it is accessible not only to readers with a knowledge of plasmas, but also to scientists familiar primarily with condensed matter, particularly in the field of complex fluids. Accordingly, we will introduce here some of the concepts and terminology of complex plasmas.

When particles of solid matter are immersed in an ionized gas, they become electrically charged by constantly collecting electrons and ions. The charge has an equilibrium value which is typically negative. The magnitude of the charge on a micrometer-sized particle is typically several thousand elementary charges. When a large number of these particles are suspended in a plasma, one has a ''dusty plasma.'' This term originated with astronomers, who refer to the small particles in interstellar and interplanetary space as dust. More recently, some authors have referred to dusty plasmas as ''complex plasmas,'' to emphasize the similarity to complex fluids.

Charged particles in a complex plasma interact with one another through a shielded Coulomb repulsion [17,18]. In the absence of ion flow, or in a plane perpendicular to ion flow, the interparticle potential ϕ is believed to be nearly Yukawa, $\phi = (Q/r)\exp(-r/\lambda_D)$, where r is the interparticle separation and λ_D is the Debye length of the electron-ion plasma. The particles also respond to natural dc electric fields that develop in a plasma. Additional forces acting on the particle include gravity and frictional drag with neutral gas.

Complex plasma experiments in the laboratory attracted much interest after the discovery of the so-called plasma crystal. As predicted theoretically by Ikezi [19], particles suspended and confined in an ionized gas arrange themselves in an ordered structure due to their strong Coulomb repulsion. In experiments [20–24] particles are found levitated in a sedimented layer at the bottom of the plasma, above a horizontal electrode. They settle at an equilibrium height where gravity is balanced by an upward electrical force. A sufficient electric field occurs in a non-neutral boundary layer, called a sheath, located above a horizontal electrode operated with a negative dc electric potential. A slight bowl-shaped curvature in the sheath provides external confinement of the particles in the radial direction. Thus, the suspension of repulsive particles is trapped in all directions. They arrange themselves in a lattice, which can have either single or multiple horizontal layers. In the horizontal plane the par-

ticles generally arrange themselves in a triangular lattice with sixfold symmetry.

Laboratory complex plasmas are nonequilibrium systems. Electrons and ions are continuously lost to the boundaries, and in a steady state they must be replenished constantly by ionization of the neutral gas. Sustaining the plasma requires a constant energy input, in the form of electrical power applied to a pair of electrodes. The kinetic temperature of the microspheres, electrons, ions, and neutral gas atoms are in general not equal.

The phase state of a complex plasma is determined mainly by two dimensionless parameters. The first is the interaction range a/λ_D, where a is the particle spacing and λ_D is the Debye length, is usually of the order of unity. The second is the Coulomb coupling parameter Γ, which is the ratio of the interparticle potential energy and the particle thermal kinetic energy [19]. This parameter can vary over many orders of magnitude, depending on the particle size and the particle kinetic temperature. In general, when $\Gamma > 1$, the complex plasma is said to be ''strongly coupled'' and it behaves like a liquid or, at extreme values of Γ, like a solid, with particles arranged in a crystalline lattice [19]. Otherwise they behave like atoms in a gas. It was shown that such crystals can undergo phase transitions [15,24–27]. It is possible to suspend particles in a monolayer. The particles never touch one another in this system.

Like other condensed matter systems, strongly coupled complex plasmas can sustain waves. For small wave amplitudes, the interparticle forces can be linearized to derive a wave equation. In all cases there is a compressional wave, and in the case of a solid in two or three dimensions there is also a transverse or shear wave. In the field of complex plasmas, i.e., dusty plasmas, the compressional wave is termed the dust lattice wave (DLW) [28–30] if the interaction range $a/\lambda_D \gg 1$, or the dust acoustic wave (DAW) [31–33] if $a/\lambda_D \ll 1$. The DAW also propagates in weakly coupled complex plasmas [34].

For waves in a two-dimensional lattice with a Yukawa interparticle potential [35], Peeters and Wu [36] derived a phonon spectrum, and found the longitudinal and transverse wave velocities for a two-dimensional colloidal lattice. Their theory considers the no-damping case. The compressional wave is faster than the transverse wave by a factor of approximately 2 for $a/\lambda_D > 4$. This factor increases to approximately 7 for $a/\lambda_D = 1$. For $a/\lambda_D \ll 1$ the transverse wave velocity remains constant, while the compressional wave velocity increases as $1/\sqrt{a/\lambda_D}$. The dispersion relation for the compressional wave in two dimensions including the effects of damping was derived by Homann *et al.* [29].

Because of its higher speed, the compressional wave will be responsible for most or all of the features of the Mach cones that we will report in this paper. The slower speed of the shear wave means that its wave energy is concentrated within a much smaller angle than the angle for the compressional wave in Fig. 1. The compressional wave has no dispersion, i.e., the frequency is linear with wave number, except at large wave numbers. This property of having no dispersion allows disturbances over a wide range to propagate outward at the same speed, a condition that is essential for the production of a Mach cone.

The existence of Mach cones in complex plasmas was originally predicted by Havnes *et al.* [2,3]. They described how a charged body moving through a cloud of charged particles can excite the DAW. If the body moves faster than the dust acoustic speed, the waves will form Mach cones. As a specific example, Havnes *et al.* carried out calculations predicting that Mach cones are produced in the layers of dust in Saturn's rings. This dust is charged by exposure to the Saturnian magnetospheric plasma. Charged dust particles rotate about the planetary axis at the same angular velocity as the planet itself, whereas boulders move in Keplerian orbits at a different speed. The difference in these two speeds is supersonic, compared to the acoustic speed in the charged dust. It is anticipated that when the Cassini spacecraft arrives at Saturn in 2004, its cameras might possibly be able to image Mach cones in the rings.

III. APPARATUS

A. Plasma

The plasma in our experiments was a capacitively coupled radio-frequency discharge. The discharge apparatus shown in Figs. 2(a) and 2(b) includes a lower aluminum disk electrode 230 mm in diameter. A 13.56-MHz rf generator was connected to the lower electrode through an impedance matching network and a coupling capacitor. A grounded upper ring and the vacuum vessel walls served as the other electrode. The matching network was adjusted to achieve a minimal reflected power, typically much less than 1% of the forward power. The resulting rf high voltage sustained the plasma discharge. Argon, krypton, or xenon gas was admitted to the chamber at a 0.5-6 sccm rate, and a constant pressure of 1.2 Pa was regulated with a servo valve between the chamber and the turbo pump.

The lower electrode was designed with a 2-mm rim to provide a slight bowl-shaped curvature to the plasma sheath, which conforms in shape to the electrode. This curvature yields a weak radial force on negatively charged particles, pushing them toward the central axis of the electrode configuration.

The Debye length λ_D was measured using a Langmuir probe, i.e., a metal wire, inserted into the plasma. A current-voltage characteristic curve was recorded and this was used to determine λ_D using the ABR method [37]. It also provided a measurement of the electron temperature T_e and ion density n_i. The probe was at a height of 15 mm above the lower electrode, which is higher than the plasma sheath boundary. The probe tip was designed to avoid common sources of errors in probe measurements, including contami-
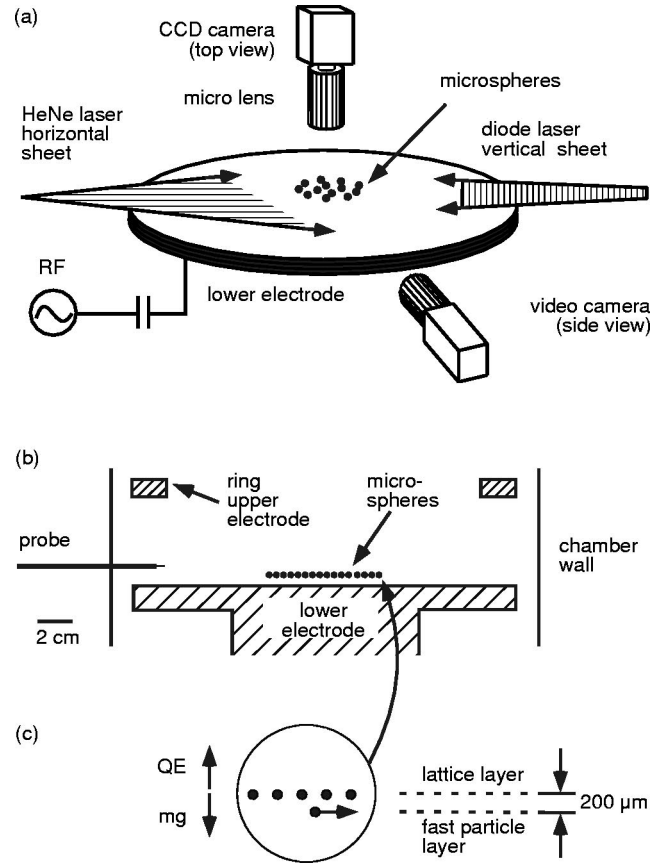

FIG. 2. Apparatus: (a) sketch in an oblique view, (b) scale drawing in a side view, and (c) locations of the two-dimensional crystal layer and the the incomplete second layer 200 μm below. Particles in the latter layer moved at supersonic speeds, creating Mach cones in the main layer. Reprinted from Ref. [4].

nation of the probe tip and insulator, too large a probe size, rf distortion, and low-frequency noise and drift [38,39]. It had passive rf compensation, with a reference electrode connected to the probe tip by an internal shunt capacitor. It also had internal choke inductors to suppress rf current at 13, 26, and 40 MHz.

The discharge parameters are listed in Table I. In our experiment the temperature of neutrals T_n and ions T_i were believed to be equal to room temperature, while the electron temperature T_e was much higher, of the order of 1 eV. In the main plasma region, where the probe was inserted, $n_e = n_i$. However, in the sheath, where the particles were levitated, $n_e \neq n_i$. Moreover, n_i is reduced in the sheath compared to the main plasma region. To adjust our measurements for

TABLE I. Discharge conditions.

Discharge conditions	1	2	3	4	5	6
Gas	Xe	Xe	Kr	Kr	Ar	Ar
Power (W)	50	100	50	100	50	100
Self-bias voltage (V)	260	380	260	380	260	390
Plasma potential (V)	9	10.5	10.5	11	10.5	11
Electron temperature (eV)	0.6	0.7	1.1	1.1	1.6	1.6
Ion density (10^9 cm^{-3})	5.1	7.9	2.5	3.5	1.4	2.2
Debye length at probe height, λ_D (μm)	80	70	160	140	250	200

TABLE II. Structural parameters for the crystals made of 8.9 ± 0.1 μm particles. Discharge conditions are found in Table I.

Discharge conditions	1	2	3	4	5	6
Number of events analyzed	7	4	5	6	5	7
Particle separation, a (μm)	335 ± 3	298 ± 2	481 ± 2	450 ± 2	586 ± 5	578 ± 9
Translational order length, ξ/a	2.8 ± 0.2	1.8 ± 0.1	2.7 ± 0.1	3.3 ± 0.3	3.9 ± 0.7	3.0 ± 0.3
Orientational order length, ξ_6/a	4 ± 1	1.3 ± 0.1	4 ± 2	11 ± 1	8 ± 4	5 ± 2
Fraction of sixfold cells	77 ± 3	66 ± 2	74 ± 2	83 ± 1	84 ± 4	83 ± 3
Particle height (mm)	5.7	5.9	7.4	8.0	8.8	9.3
Epstein drag (s^{-1})	2.9	2.9	2.3	2.3	1.6	1.6

these factors, we introduce a density reduction factor estimated to have a value of 3. Since $\lambda_D \propto 1/\sqrt{n_i}$, the resulting Debye length in the sheath is larger by a factor of $\sqrt{3}$. We use this factor when reporting the interaction range a/λ_D.

B. Particles

After igniting a plasma, we introduced monodisperse polymer spheres. They were shaken from a dispenser that we inserted into the vacuum vessel at a height above the electrodes. We used spheres of two different sizes 8.9 ± 0.1 μm or 4.808 ± 0.112 μm. The particle mass density was 1.51 g/cm^3. We thoroughly cleaned the particle shaker with acetone and replaced the wire mesh before recharging the shaker with the particles of a different size in order to avoid contamination.

Immersed into the plasma, the particles charged negatively and levitated in the electric field of the plasma sheath. They formed a monolayer suspension, about 4 cm in diameter, with particles arranged in a hexagonal lattice.

The particle motion was strictly two dimensional. We verified this by imaging particles at a high magnification, using a long distance microscope that had a 1 mm^2 field of view. The vertical motion amplitude did not exceed 10 μm, which is of the order of the particle size, and insignificant compared to the interparticle spacing.

C. Method of generating cones

The Mach cones in this experiment were generated spontaneously. When the particle cloud diameter exceeded a critical value (approximately 1–2 cm), a few of the particles formed a second incomplete layer below the main layer [see Fig. 2(c)]. The particles in the lower layer moved horizontally at a speed of 30–60 mm/s. The supersonic particles moved at almost constant speed until they reached the radial edge of the main layer, where they turned around. Sometimes they spontaneously changed direction in midflight, but mostly they moved in straight lines. The acceleration mechanism responsible for this motion remains a mystery, although we can speculate that it may be related to disturbances in the so-called ion wakefield, i.e., the ion flow downstream of the main layer.

Because these supersonic particles are charged, they scattered the particles in the main layer above them, via a screened Coulomb interparticle potential. This scattering was the disturbance that launched the Mach cones. In this paper we present images of cones that were generated by particles that moved in a straight line and at a constant speed. Typi-

cally we observed several supersonic particles in the whole lattice, and they crossed the camera field of view a few times per second.

D. Imaging

To visualize the particles we illuminated them with a laser beam expanded into a sheet with a cylindrical telescope, and we imaged them with a monochrome video camera operated at 25 frames/sec. The camera was equipped with an interference bandpass filter to select the laser light. The top view was obtained with a vertically mounted camera and a 85-mm f1.4 Nikon lens. A horizontal He-Ne laser sheet illuminated the particles. The field of view was 150–230 mm^2 and covered 1000–3000 particles. We obtained the side view using a horizontally mounted long-distance microscope with a video camera and a vertical diode laser sheet. Only 2–5 particles were in the field of view, which was about 1 mm^2. The video fields were recorded on an SVHS video recorder and then digitized for a computer analysis. Interlaced video frames were separated into two fields, so that the data that we present in this paper has a time resolution of 50 video fields/sec.

IV. IMAGE ANALYSIS METHOD

In contrast to shock experiments in gas dynamics and solids, where the medium is imaged as a continuum, here our raw data is a movie showing the individual particles. This allows us to analyze the microscopic dynamics of particles as they move in response to the disturbance. It is also possible to produce smoothed images showing continuum quantities such as particle number density. We can thus provide a wide variety of results from our video. These results require more effort to prepare than, for example, a Schlieren photograph of a shock wave in a wind tunnel. Here we will review our image analysis methods.

The methods all begin with the identification of individual particles in a single video field. First, the gray-scale image was converted into a black-and-white image by applying a threshold. We then searched for connected pixels. A particle's x-y coordinates were computed as the center of the connected pixels, when weighted by their brightness. In the next step, particles were tracked from one field to another to yield their trajectories in time. Two consecutive fields were used to determine the particle velocities.

Velocity vector maps were then plotted. In producing the maps, vectors were drawn with a length equal to 10 times the difference in the particle position in one video field com-

TABLE III. Structural parameters for the crystals made of 4.8 ± 0.1-μm particles. Corresponding discharge conditions are listed in Table I.

Discharge conditions	1	2	3	4	5
Number of events analyzed	7	14	8	7	5
Particle separation, a (μm)	360 ± 2	328 ± 3	429 ± 4	356 ± 2	726 ± 6
Translational order length, ξ/a	2.7 ± 0.4	3.1 ± 0.4	2.5 ± 0.3	3.9 ± 0.6	2.2 ± 0.3
Orientational order length, ξ_6/a	4.1 ± 0.6	8 ± 3	3 ± 1	13 ± 11	1.9 ± 0.6
Fraction of sixfold cells	74 ± 4	80 ± 3	68 ± 4	83 ± 5	63 ± 6
Particle height (mm)	6.7	7.2	7.8	8.4	9.4
Epstein drag (s^{-1})	5.4	5.4	4.3	4.3	3.0

pared to the next. This was repeated for a series of video fields where a Mach cone could be identified moving through the image. Examining the vector maps, we manually measured both the x-y coordinates of a cone's vertex coordinates and the cone angle μ. Using the vertex coordinates, the velocity of the supersonic particle V was computed for every field, averaged for every experimental run, and the error was calculated.

We also prepared gray-scale maps of speed as a continuum quantity. To improve the signal-to-noise ratio, we averaged these maps over several consecutive fields. We did this by aligning multiple consecutive fields of the vector maps so that the cone's vertex had the same position in each field. We then calculated the absolute value of velocity for every particle, interpolated the resulting irregular array onto a regular grid and applied a smoothing 2D filter. This yielded the composite high resolution gray-scale images of the absolute value of the velocity that we present later.

We identified interparticle bonds by Delaunay triangulation. This was used for several purposes. One application was defect analysis. We identified defects as particles with a number of bonds not equal to six.

Another application of the Voronoi maps was a calculation of the local particle areal density, which is a continuum quantity. This was calculated as the inverse area of the Voronoi cells. Gray-scale images of the areal number density were produced using the overlay technique described above.

To characterize how highly ordered our lattice was, we carried out standard structural analysis methods. We calculated the pair correlation function $g(r)$ and the bond orientation correlation function $g_6(r)$ [40] from the particle coordinates and triangulation maps, respectively. These correlation functions were calculated for images that were not affected by Mach cones, so that they represent the undisturbed medium. Fitting these correlation functions yielded the particle separation a, determined as the position of the first peak of the pair correlation function, as well as the correlation lengths for exponential decay of these functions.

To determine the particle kinetic temperature, we measured the particle velocities from 200 fields using the side view video with a high magnification so that only 2–5 particles were in the field of view. The particle velocity had two components, random and drift. The drift velocity $\langle v \rangle$ was approximately constant, so that we were able to subtract it when computing the random particle motion. The kinetic temperature was computed as $T = m \langle (v - \langle v \rangle)^2 \rangle / k_B$, where m is the particle mass, v is the measured particle velocity,

$\langle (v - \langle v \rangle)^2 \rangle$ is the average square random velocity, and k_B is the Boltzmann constant.

V. EXPERIMENTAL PARAMETERS FOR THE TWO-DIMENSIONAL YUKAWA SYSTEM

The properties of the lattice of particles in our two-dimensional suspension are presented here. Conditions varied slightly, depending on the particle diameter and the type of gas used in the discharge. All the measured parameters are listed in Tables II and III, for 8.9 μm and 4.8 μm diameter particles, respectively.

The lattice was hexagonal, with a considerable number of defects. The fraction of sixfold coordination numbers varied from 63 to 84 %, depending on the experimental parameters. Defects consisted primarily of five- and sevenfold coordinated vertices on the Voronoi map.

The correlation functions for typical operating conditions are shown in Fig. 3. These functions exhibit an order that is typical of a solid with a fair degree of disorder. They are much more highly ordered than a liquid. The correlation length is the distance at which the structural order in the correlation function decreases by one e folding. Larger values of these lengths indicate a more highly ordered system.
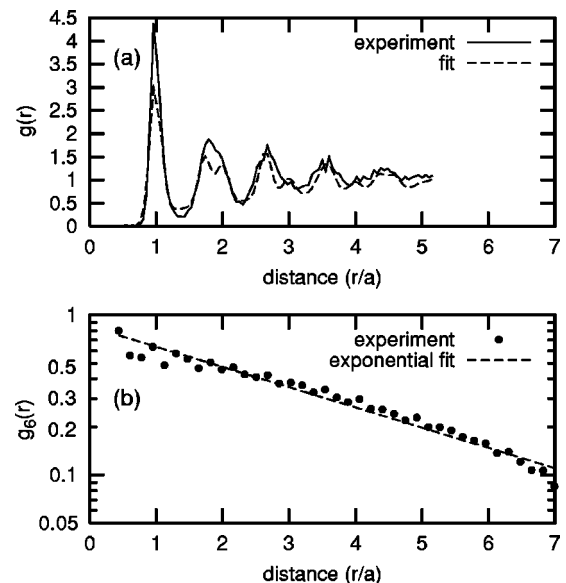

FIG. 3. (a) Pair correlation function and (b) bond orientation correlation function for 8.9-μm particles in an argon 100-W discharge.

TABLE IV. Experimental parameters for the crystals made of 8.9 ± 0.1-μm particles. Discharge conditions are found in Table I. Here the terms first and second refer to the two cones. The acoustic velocity was computed from the Mach angle using Eq. (1).

Discharge conditions	1	2	3	4	5	6
Acoustic velocity (first) (mm/s)	21.1 ± 0.2	20 ± 1	19 ± 2	18.9 ± 0.2	20 ± 1	18 ± 1
Acoustic velocity (second) (mm/s)	15 ± 1	14 ± 2	14 ± 5	13 ± 1	15 ± 1	13 ± 3
Particle charge, Q	15 000	14 000	14 000	14 000	14 000	14 000
Interaction range, a/λ_D	2.3	2.4	1.8	1.9	1.4	1.7
Kinetic temperature (K)	3 600	4 100	2 500	3 600	1 400	1 700
Coupling parameter, Γ	3 000	2 500	2 700	1 900	4 000	3 000

The translation correlation length ξ was found to be in the range $(1.8-3.9)a$, while the orientation correlation length ξ_6 varied more significantly $(1.3-13)a$. The large variance of the orientation correlation length within the same operating conditions suggests that the particle cloud was not uniform and had patches of higher and lower order.

The damping rate from the gas drag was calculated using the Epstein method [41,42]. It had values in the range 1.6– 5.4 s^{-1}, which is five orders of magnitude smaller than for particles of the same size in water. This low damping rate allowed us to produce Mach cones. The damping rate increases with atomic mass from argon to krypton to xenon, and it decreases with increasing particle size.

Additional parameters characterizing the Yukawa interparticle potential are the interaction range a/λ_D and the particle charge Q. The latter was determined from the Mach cones, using a method that will be explained later. These values are presented in Tables IV and V. The interaction range was in the range 1.4–2.7. The charge was typically $-14\,000e$ and $-5\,000e$, for 8.9 μm and 4.8 μm particles, respectively.

VI. MACH CONES IN 2D SOLIDS

While Mach cones are clearly visible on a video, it is difficult to spot them on a still picture. Figure 4(a) shows the particle positions as the cone passes by. One can see a rarefaction caused by the cone vertex in the middle upper part of the figure.

The Mach cone is more easily identified on a particle velocity vector map, Fig. 4(b). The supersonic particle in this case was moving from left to right. It is clearly seen that the cone has a double structure, with the particles moving forward in the first cone and backward in the second. The spacing between the cones is about $(8-20)a$.

The first cone has a rounded vertex. We attribute this to

the finite size of the perturbation. This phenomenon is well known in gas dynamics, where a finite-sized object, such as a sphere, creates a Mach cone with a rounded vertex, while a pointlike disturbance produces a sharp V-shape vertex. In our experiment the supersonic particle is surrounded by its Debye sphere, which has a scale length λ_D. It is over this finite length that the supersonic interacts with the particles in the lattice layer above it. We believe this accounts for the rounded vertex of our first cone. The second cone, on the other hand, has a sharp tip. We will make some further comparisons of the angles of the two cones later in this paper.

Gray-scale speed maps, Fig. 4(c), also show the cones clearly. The double cone structure is visible as two dark cones on a brighter background. The background is not white, as one would expect for zero velocity. This is due to thermal and collective particle motion, where the latter can include drift of the suspension as a whole, local flows within the suspension, and waves.

Speed maps can be compared to number density maps, Fig. 4(d). This comparison shows that the first and second cones are regions of compression and rarefaction, respectively. We attribute the rarefaction wave to a restoring force due to the interparticle interactions in a crystalline state. A distinctive rarefaction wave like this would not occur in a gas, where the atoms have no memory of their original positions. The rarefaction wave does have an analog in solids, however. It is similar to the release wave in solids, which occurs after the passage of a shock [1].

We repeated the experiment using different gases and two different particle sizes. Mach cones for the series of experiments with 8.9-μm particles are shown in Fig. 4 for argon, Fig. 5 for krypton, and Fig. 6 for xenon. The length of the cone decreases as the gas atomic mass increases, from argon to krypton to xenon. Note the different size scale in the images for these different gases.

Comparing Mach cones made using two different particle

TABLE V. Experimental parameters for the crystals made of 4.8 ± 0.1-μm particles. Here the terms first and second refer to the two cones. Run 6 is not shown: the particle cloud was unstable. Discharge conditions are found in Table I.

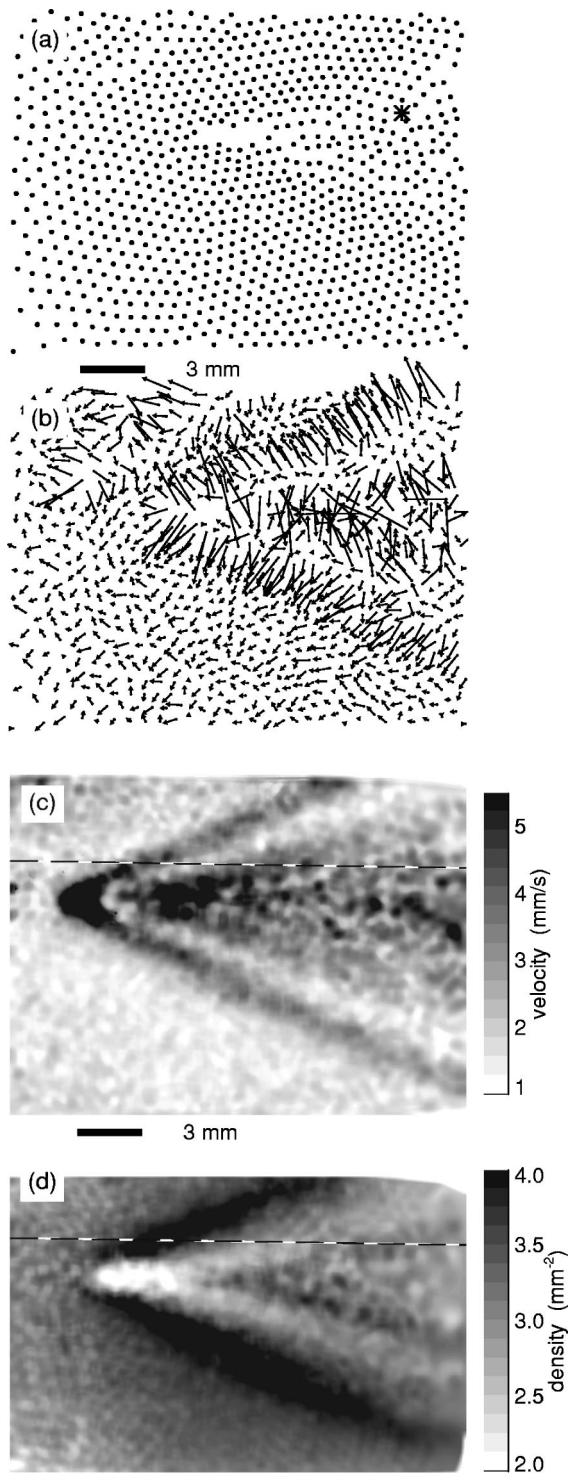| Discharge conditions	1	2	3	4	5
Acoustic velocity (first) (mm/s)	18 ± 3	20 ± 5	20 ± 2	22 ± 1	13.0 ± 0.3
Acoustic velocity (second) (mm/s)	13 ± 3	14 ± 6	13 ± 1	16 ± 1	n/a
Particle charge, Q	5 400	6 000	4 900	5 000	4 400
Interaction range, a/λ_D	2.5	2.7	1.6	1.5	1.7

FIG. 4. Mach cone with 8.9-μm particles in an argon 100-W discharge. The supersonic particle moved to the left. (a) Particle positions for a single video field, (b) particle velocity vector map derived from particle positions in two consecutive video fields, (c) gray-scale speed map, and (d) gray-scale number density map. The latter two maps were averaged from data for ten video fields. The asterisk (*) (a) marks the particle for which the trajectory is plotted in Fig. 9. The dashed lines (c), (d) indicate the location of the cross-sectional slices of velocity and density profiles that are plotted in Fig. 11. The first cone consists of particles moving forward, and it coincides with the high density region. The second cone has particles moving backward, and it coincides with the low density region.
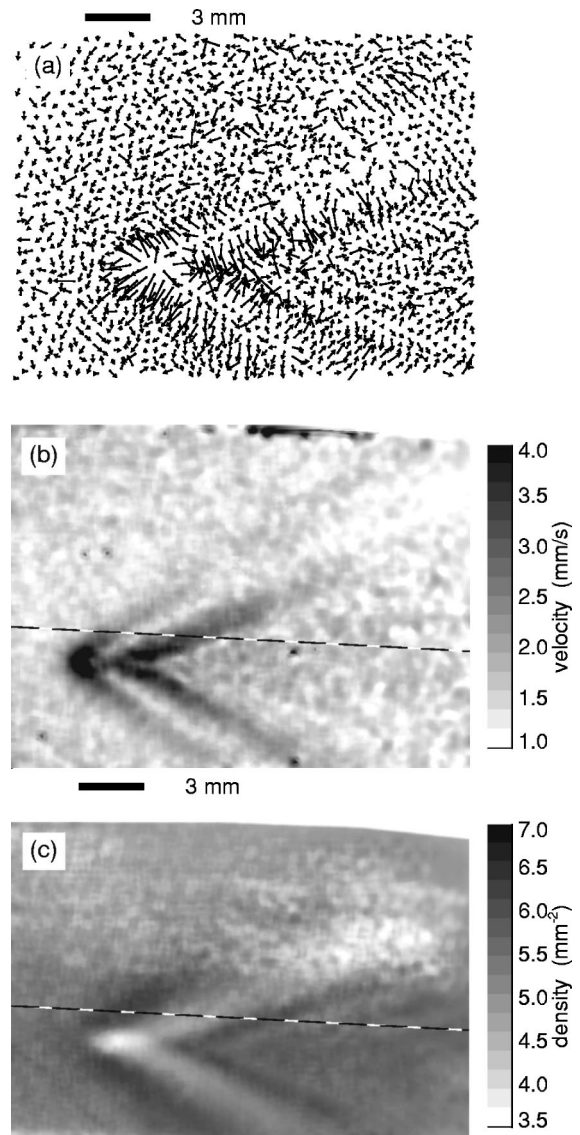
FIG. 5. Mach cone with 8.9-μm particles in a krypton 100-W discharge. The supersonic particle moved to the left. (a) Particle velocity vector map derived from particle positions in two consecutive video fields, (b) gray-scale speed map, and (c) gray-scale number density map. The latter two maps were averaged from data for 20 video fields. The dashed lines (b), (c) indicate the location of the cross-sectional slices of velocity and density profiles that are plotted in Fig. 12. The Mach cone is less distinct than in argon.

sizes, we find that those made with 4.8-μm particles (Fig. 7) are longer and have sharper vertices than for 8.9-μm. We have no explanation for the latter result.

Now we present a test of the Mach angle relation, Eq. (1). This is one of the chief results of this paper. For one set of experimental conditions (Kr, 100 W, 4.8-μm particles) we were able to measure cones created by supersonic particles where some had a faster speed and others were slower, over a range of nearly a factor of 2. For each of these events, we measured the cone angle μ manually from the vector velocity maps. Figure 8 shows $1/\sin\mu$ as a function of the supersonic particle velocity V. Note that the data generally fall on a straight line passing through the origin. This result is consistent with the Mach angle relation, Eq. (1).
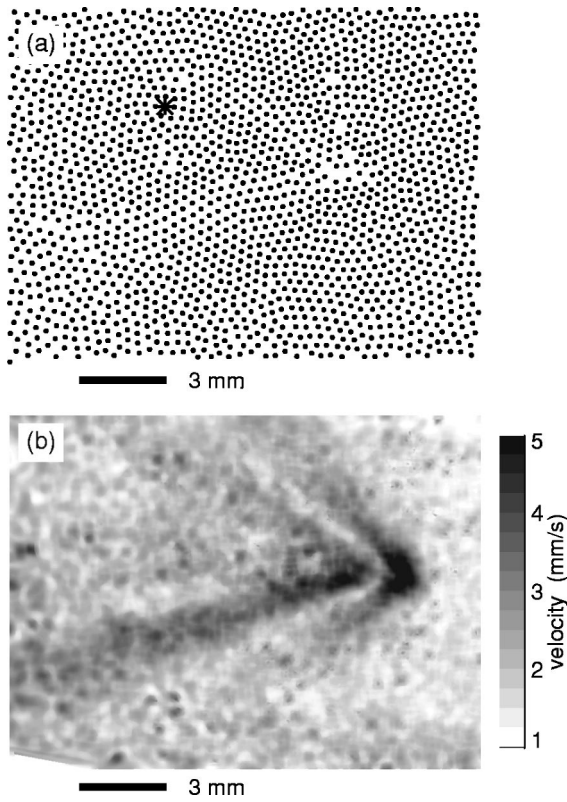
FIG. 6. Mach cone 8.9-μm particles in a xenon 50-W discharge. The supersonic particle moved to the right. (a) Particle positions for a single video field, (b) gray-scale speed map averaged from data for 16 video fields. The asterisk (a) marks the particle for which the trajectory is plotted in Fig. 10. The Mach cone is less distinct than in argon and krypton.

The slope of the straight line in Fig. 8 yields a measurement of the wave's acoustic speed. In this experiment, the first cone had a faster speed of 20 mm/s, while the second cone had a slower acoustic speed of 13 mm/s.

We expect that the angle of the first cone should correspond to the speed of a compressional wave in the undisturbed medium. This is because it is propagating outward into a medium that has not yet been disturbed by a shock. It is possible that the angle of the second cone might be determined by nonlinear effects. We suggest this because the second cone lies in the medium that was disturbed by the first cone. If the angle of the second cone is determined by the local continuum parameters, such as the number density (as discussed in Sec. VIII A), and if these parameters were disturbed by the first cone, then one would expect that the angle of the second cone should depend on the magnitude of the disturbance created by the first cone. We are unable to test this idea in the present experiment, because we had no way to vary the intensity of the disturbance, but perhaps a test can be carried out in future experiments or numerical simulations.

Since the Mach cones in our experiment propagate through a solid medium, which can sustain both compressional and shear waves, it is reasonable to ask whether both waves might be present. The theoretical model of Ref. [36] for a two-dimensional Yukawa crystal predicts that the shear wave is slower than the compressional wave by a factor of 4 to 7, for the range of a/λ_D in our experiment. This means
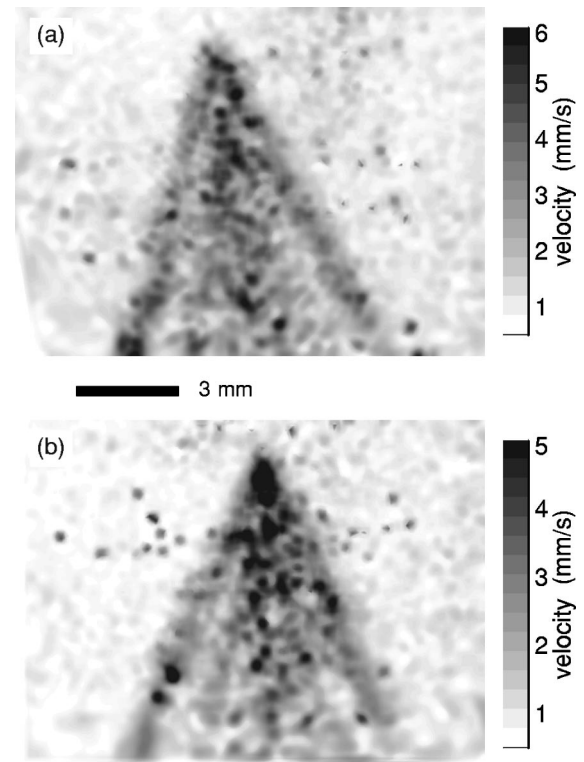

FIG. 7. Speed maps of Mach cones with 4.8-μm particles (a) krypton and (b) xenon 100-W discharges. The cones are more distinct and have sharper vertices than for the same discharge conditions with the larger 8.9-μm particles.

that only within a very narrow angle can the disturbance include particle motion corresponding to the shear wave. Therefore, the first cone, and most or all of the second cone, must be due solely to compressional wave motion.

To further analyze the particle motion in our experiment, we prepared time series and maps of the orbits of some representative particles. We selected particles on the cone path slightly off the axis. These particles are marked with an as-
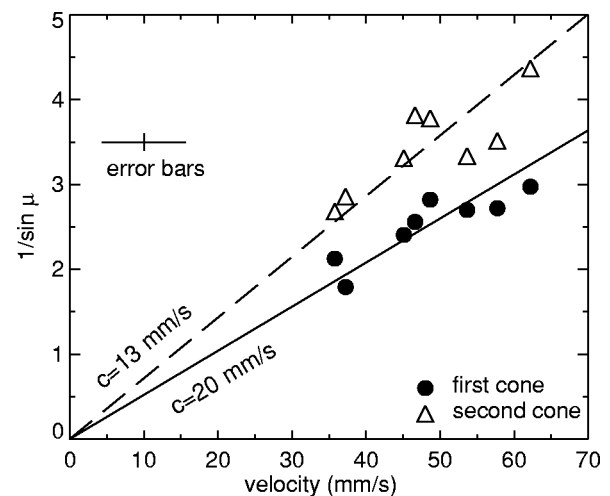

FIG. 8. Test of the Mach angle relation, Eq. (1). Here $1/\sin \mu$ is plotted vs the velocity V of the supersonic particle. Data are for 4.8-μm particles in a 100-W krypton discharge. The straight lines correspond to the acoustic velocities for the cones. The first cone has a faster acoustic velocity than the second.
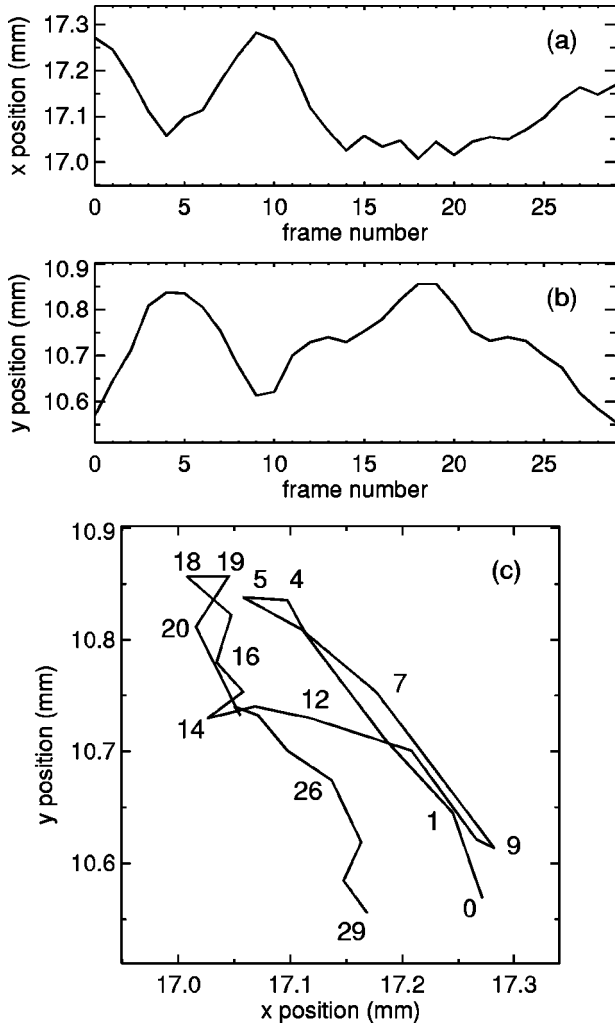
FIG. 9. Orbit of one particle, as marked with an asterisk on Fig. 4(a). Time series are shown for (a) x and (b) y positions. (c) A map of the trajectory is shown. The numbers 0–29 denote the video field number, which indicates the time sequence. The particle exhibits nearly oscillatory motion superimposed on a secular drift.

terisk (*) in Figs. 4(a) and 6(a). In both cases, particle motion is an oscillation superimposed on a secular drift, as shown in the time series in Figs. 9(a), 9(b), 10(a), and 10(b). Maps of these same particle orbits are shown in Figs. 9(c), 10(c). It seems that in argon discharge particle motion is less damped [Fig. 9(c)] than in xenon [Fig. 10(c)].

VII. SHOCKS IN 2D SOLIDS

Here we will show that the disturbances in our Mach cones can be analyzed as shocks. We do this using our experimental data in the theoretical Hugoniot relations for shocks.

To visualize the interior structure of our shocks, we plotted cross-sectional slices of the velocity and density maps along a line parallel to the direction of the cone propagation. The locations of these slices are indicated with a dashed line in Figs. 4(c) and 4(d) for the case of argon discharge. Profiles of number density, velocity in the direction parallel and perpendicular to the slice are shown in Figs. 11(a)–11(c), respectively. The particle number density increase at 6 mm is
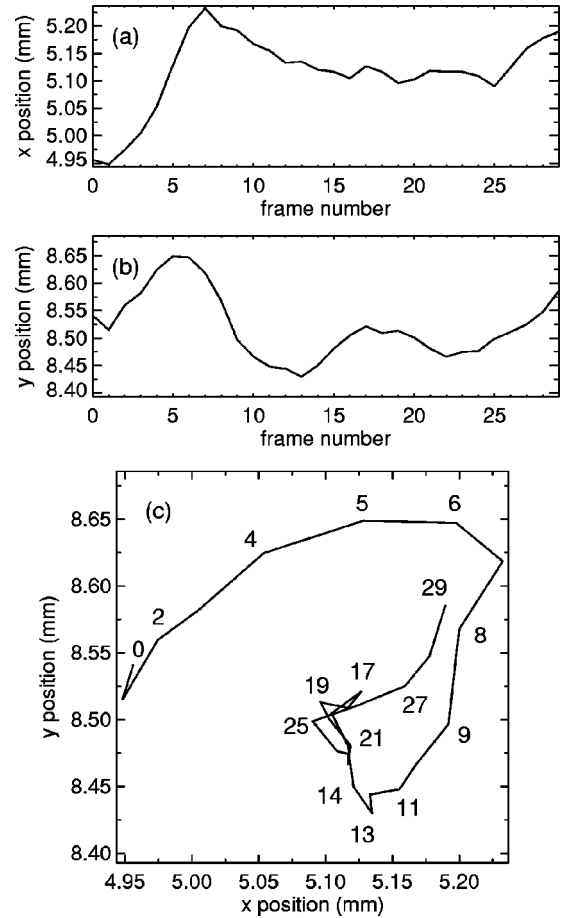

FIG. 10. Orbit of one particle, as in Fig. 9. The particle is the one marked with an asterisk in Fig. 6(a). This case shows higher damping.

accompanied by a rise in the particle velocity. This corresponds to the first cone, which is compressional shock motion. It is followed by the density drop at 12 mm where the velocity peaks in the opposite direction. In krypton (Fig. 12), the parameters rise more steeply, they exhibit more oscillations, and the density drop is more pronounced.

The shock thickness is an important characteristic length for shocks. Normally it is of the order of a few mean-free paths [5], which in a crystal would be of the order of the particle spacing a. In our experiment, the velocity and density rise in a gradient with a scale length of 2–3 mm. This distance corresponds approximately to $(3-5)a$.

Shock waves satisfy the Hugoniot relations [5]. These are derived from the conservation laws assuming that there is a jump in the number density and other continuum parameters. Assuming that there is no motion ahead of the shock, the Hugoniot relations [5] for a linear shock in two dimensional geometry are

$$n_2(U-v_{\perp 2})=n_1 U, \tag{2}$$

$$mn_1 U v_{\perp 2}=p_2-p_1, \tag{3}$$

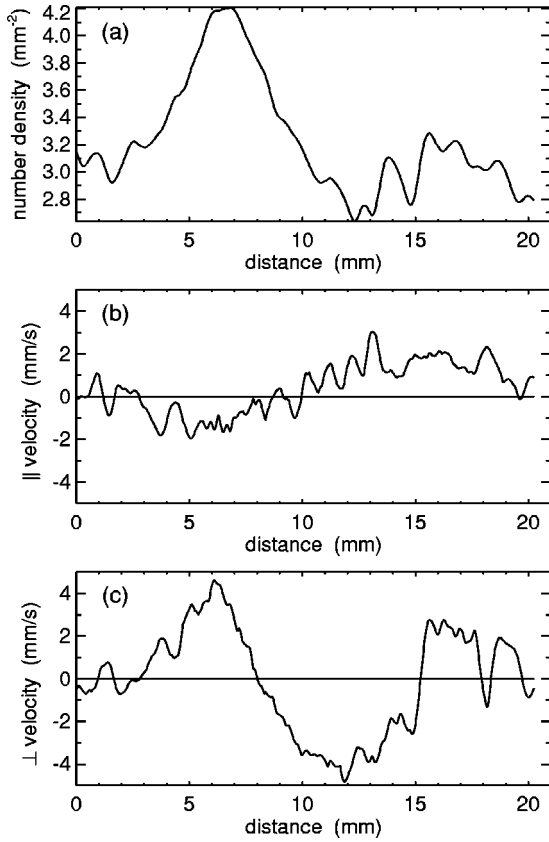$$E_2-E_1=\frac{1}{2m}(p_1+p_2)\left(\frac{1}{n_1}-\frac{1}{n_2}\right), \tag{4}$$

FIG. 11. Cross-sectional slices of (a) number density and particle velocity (b) parallel and (c) perpendicular to the direction of the supersonic particle velocity. These slices were taken from the images in Fig. 4. The number density has a peak inside the first cone at 6 mm, and this coincides with a peak in the velocity. Inside the second cone, a density minimum at 12 mm coincides with a peak velocity in the opposite direction.

where U is the shock propagation velocity, m is the particle mass, n is the two-dimensional particle number density, p is the two-dimensional normal stress, i.e., hydrostatic pressure, and E is the internal energy per unit mass. Here $\perp$ indicates the direction normal to the shock, and the indices 1 and 2 indicate the condition ahead and behind the shock, respectively. Equation (2) is based on the continuity equation. Its left- and right-hand sides were equal within 15%. This discrepancy serves as an indication of our measurement error. We used Eq. (3), which is based on the momentum equation, to calculate $p_2 - p_1$.

In order to use Eq. (4) we need to know $E_2 - E_1$. Taking into account the high value of the coupling constant Γ, we neglect the thermal energy and assume that the internal energy is equal to the potential energy. For the Yukawa interaction potential using $n \propto 1/a^2$ we have

$$E_2 - E_1 = \frac{6Q^2}{4\pi\epsilon_0 m}\left(\frac{\exp[-(a/\lambda_D)\sqrt{n_1/n_2}]}{a\sqrt{n_1/n_2}} - \frac{\exp(-a/\lambda_D)}{a}\right),$$
(5)

where Q is the particle charge, ϵ_0 is the dielectric constant, and a is the particle separation of the lattice in an undis-
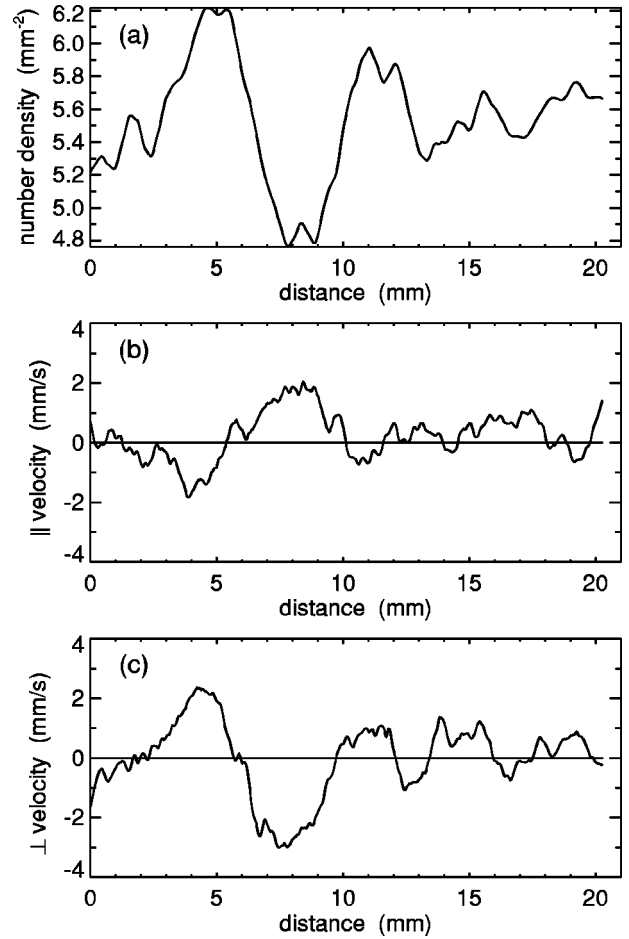

FIG. 12. Cross-sectional slices as in Fig. 11, with data taken from the images in Fig. 5(b) and 5(c). Compared to the case of argon discharge (Fig. 11) the parameters rise more steeply, they exhibit more oscillations, and the density drop is more pronounced.

turbed state (i.e., ahead of the shock). Substituting Eq. (5) into Eq. (4) we obtain $p_1 + p_2$. Thus we can compute the wave pressures p_1 and p_2.

The number density and velocity ahead and behind the shock were measured from the cross-sectional profiles. For Ar (Fig. 11), we find $n_1 = 3.0$ mm^{-2}, $n_2 = 4.2$ mm^{-2}, and $v_{y2} = 5.0$ mm/s. Substituting these values into Eqs. (2)–(5) we calculated the pressure ahead of the shock to be $p_1 = 3.7 \times 10^{-22}$ kg/s^2 and $p_2/p_1 = 1.6$. In krypton (Fig. 12), we find $n_1 = 5.3$ mm^{-2}, $n_2 = 6.2$ mm^{-2}. We then compute the pressure ahead of the shock as $p_1 = 7.1 \times 10^{-22}$ kg/s^2 and $p_2/p_1 = 1.3$.

These values of the ratio $p_2/p_1 = 1.6$ and 1.3 indicate that the shock is very weak and consequently is very close to an acoustic wave [5]. It is interesting to note that the number density varied significantly as well, with a ratio $n_2/n_1 = 1.4$ and 1.2, respectively. Because the Yukawa interparticle potential is a soft-sphere interaction, the solid can be compressed easily.

One might expect that if the disturbance created by the supersonic particle were greater, the shock might be commensurately stronger. In this experiment the disturbance was created by the fast particles moving on a plane below the lattice, and this disturbance apparently was only strong enough to create a weak shock.
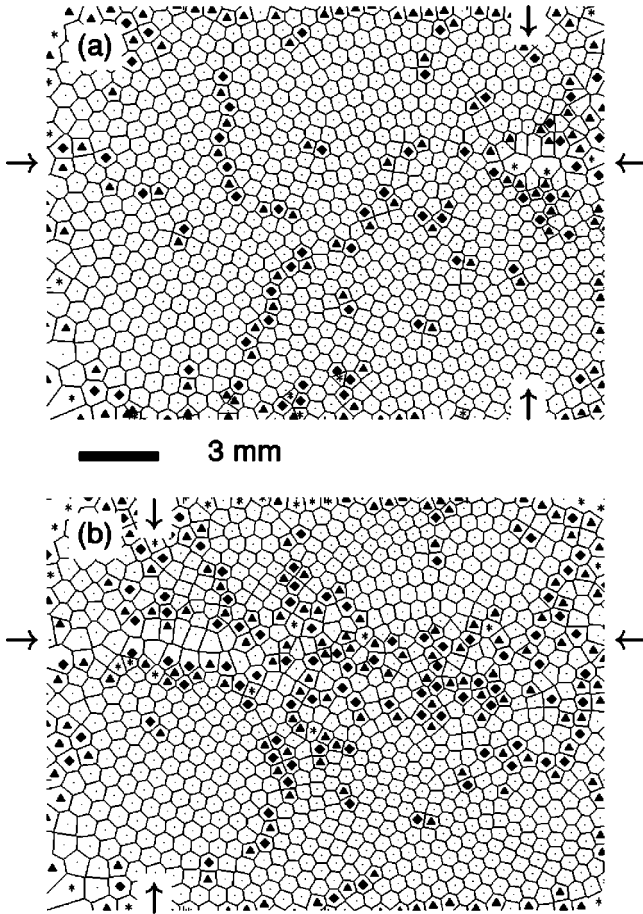
FIG. 13. Voronoi maps with 8.9-μm particles in argon 100-W discharge. Two frames are shown, separated in time by 0.24 s. The vertex, which is indicated by four arrows at the edges, moved from left to right. A narrow stripe of defects, generated in the track of the supersonic particle, indicates plastic deformation. Elsewhere no defects were generated, indicating that that deformation was elastic. Fivefold defects are marked by triangles (▲), sevenfold are marked by squares (■), and the other are marked by asterisks (*).

FIG. 14. Voronoi maps with 8.9-μm particles in krypton 100-W discharge. The two frames are separated in time by 0.26 s. In this case the Mach cone did not generate any defects, indicating that all the deformations were elastic. Fivefold defects are marked by triangles (▲), sevenfold are marked by squares (■), and the other are marked by asterisks (*).

Now we consider the issue of whether the shocks we produced are elastic or plastic. The distinction depends on whether the disturbance generates defects. Voronoi maps of the crystal lattice are shown before and after the cone has passed by in Figs. 13(a) and 13(b) and Fig. 14(a) and 14(b) for the same experimental runs as in Figs. 4 and 5, respectively. The location of the vertex of the cone is shown by arrows in each panel of these figures. In the first case (Ar, 100 W, 8.9-μm particles), there is a stripe of defects that was generated in the track of the supersonic particle, while the remainder of the lattice was untouched. In the second case (Kr, 100 W, 8.9-μm particles), the disturbance generated no defects at all. Thus we conclude that the shock waves propagating outward from the supersonic particle were elastic shocks, in the case of our experiment.

VIII. COMPLEX PLASMA DIAGNOSTICS

A. Sound speed

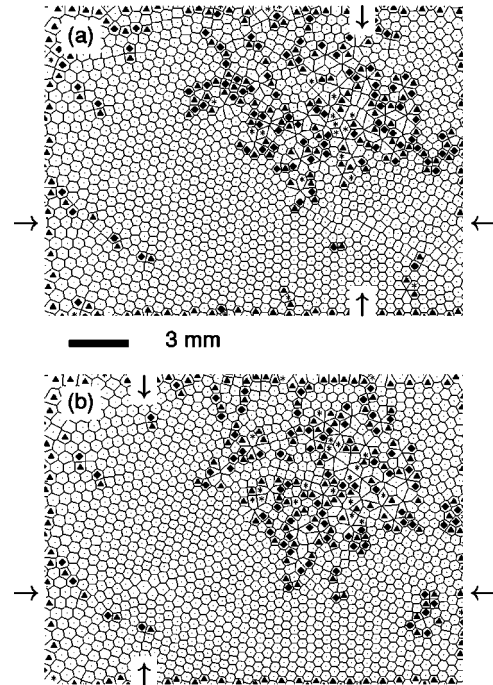The term ''dispersion relation'' refers to the relationship between a wave's frequency ω and wave number k in the linear or low-amplitude regime. Here we discuss the dispersion relation applicable to our experiment.

Like other solids, a complex plasma in a crystalline strongly coupled state can sustain both compressional and shear waves. Peeters and Wu [36] calculated the phonon spectrum, i.e., the dispersion relation in the absence of damping, for a 2D triangular lattice of particles interacting through the Yukawa potential. For long wavelengths, both the compressional and shear modes have a linear relationship between the frequency and wave number, $w \propto k$, and they are therefore characterized by an acoustic speed.

In the field of complex plasmas, the compressional wave is termed a dust lattice wave (DLW) when $a/\lambda_D > 1$. Because our experiment was characterized by $1.4 < a/\lambda_D < 2.7$, it falls in this regime. Homann et al. [29] derived the DLW dispersion relation including the effects of damping, but otherwise with the same physics assumptions as Peeters and Wu. Homann et al. also verified the dispersion relation experimentally.

Calculating the compressional wave's acoustic speed from the dispersion relation [29], if one includes only the interparticle interactions with six nearest neighbors one obtains

$$c = Q \left(\frac{A(1 + a/\lambda_D) + B(a/\lambda_D)^2}{\pi \epsilon_0 a m \exp(a/\lambda_D)} \right)^{1/2}, \tag{6}$$

where $A = 1/2$, $B = 1/4$ for a linear chain and $A = 15/32$, $B = 9/32$ for a 2D triangular lattice. For small values of a/λ_D this expression should be corrected to include more distant interparticle interactions. When these corrections are made,
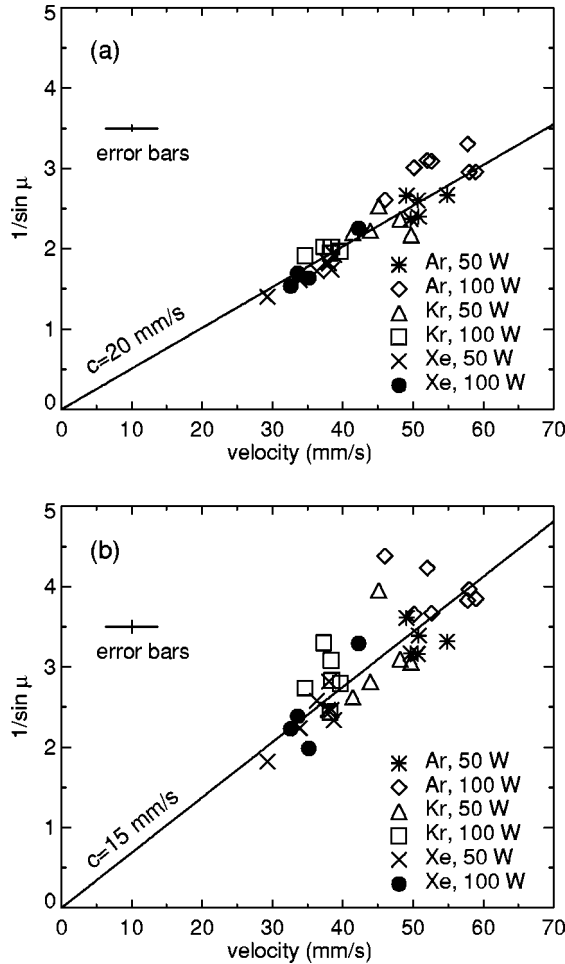
FIG. 15. Mach number ($1/\sin \mu$) vs supersonic particle velocity for 8.9-μm particles determined for the first (a) and second (b) cone at different discharge conditions. The straight lines correspond to average acoustic velocities for all events on the plot 20 mm/s (a) and 15 mm/s (b). The acoustic velocity is the same for different discharge conditions.

FIG. 16. Mach number ($1/\sin \mu$) vs supersonic particle velocity for 4.8-μm particles determined for the first (a) and second (b) cone at different discharge conditions. The straight lines correspond to average acoustic velocities for all events on the plot 20 mm/s (a) and 15 mm/s (b). The acoustic velocity is the same for different discharge conditions. It is also independent of the particle size (compare to Fig. 15).

the expression retains the same scaling with the charge and mass $Q/\sqrt{m}$ as in Eq. (6). In all cases, the acoustic speed is independent of the direction of wave propagation, just as it would be in an isotropic elastic medium [43].

While the expressions above are based on the dispersion relation for a low-amplitude linear wave, we should also discuss nonlinear effects. The acoustic velocity [Eq. (6)] has a weak dependence on particle separation. If the particle number density drops from n_1 to n_2, then the particle separation increases by a factor $\sqrt{n_1/n_2}$. The resulting acoustic velocity will decrease. In a shock wave, one would expect the compression and rarefaction of the number density to be large enough to lead to nonlinear effects such as this. To see how this applies to our experiment, let us compare the conditions in the most compressed and the most rarefied regions of the lattice. The acoustic velocity varies by 16% in argon, and by 10% in krypton in these two extremes, as calculated for the density change from maximum to minimum in Figs. 11(a) and 12(a).

While we presently have no quantitative model to predict the angle of the second cone, the parameters described above suggest that nonlinear effects, depending on the amplitude of
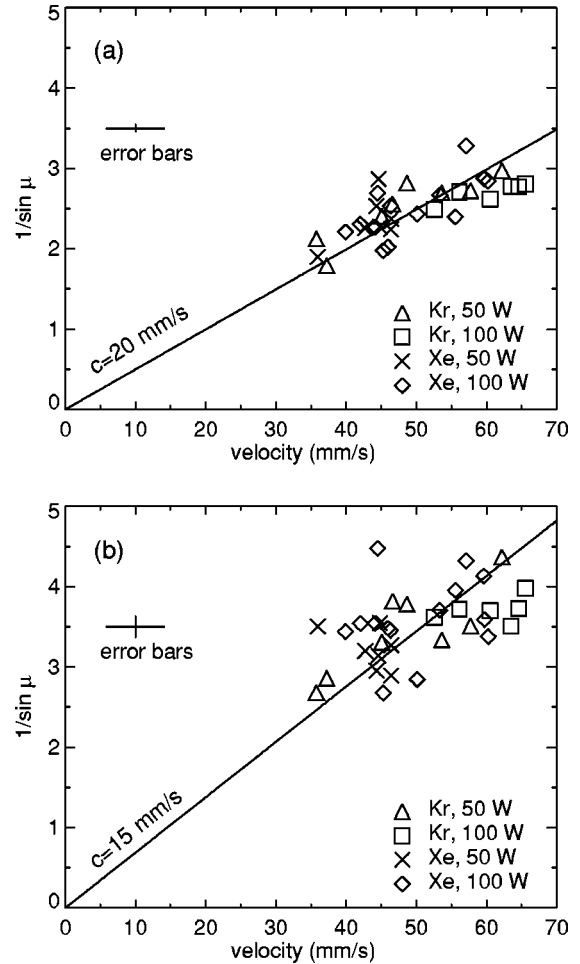
the disturbance created by the supersonic object, might need to be taken into account.

Finally, we should also note an empirical result that says something about the conditions of the complex plasma. In all the discharges we tested, the acoustic speed was the same, and it was independent of the particle size. This result can be seen in Figs. 15(a) and 16(a). These show $1/\sin \mu$ for the first cone, which we interpret as V/c, as a function of the supersonic particle velocity V. These data for all the discharge conditions lie on the same straight line, indicating that all the discharge conditions have the same acoustic speed, within the error bars. Moreover, the acoustic speed for the second cone is also the same regardless of the plasma conditions. The speed for the second cone was 25% slower than for the first.

The only exception to our result that the acoustic speed is independent of discharge conditions was the crystal of 4.8-μm particles in argon at 50 W. While not shown in Figs. 15 and 16, these results are listed as experimental condition (5) in Table V. The acoustic speed for the first cone [Figs. 15(b), 16(b)] was somewhat lower for this case, while the

particle separation was almost twice as high as in the other cases. The second cone could not be positively identified for this condition.

B. Dissipation

The waves constituting the Mach cones decay at some distance from the vertex. One of the reasons is the gas drag that slows down the oscillating particles and dissipates the wave energy. This drag applies a force $F = M v \nu_d$, where M and v are the particle mass and velocity, respectively, and ν_d is the damping rate. The corresponding length scale, for the wave energy to diminish by a factor $1/e$, is $l = c/\nu_d$.

The damping rate for a sphere moving through a rarefied gas can be computed using the Epstein drag expressions [41,42] as

$$\nu_d = \sqrt{\frac{8}{\pi}} \frac{\delta P}{\rho_d r_d} \sqrt{\frac{M_g}{k_B T_g}},$$

where δ is a numerical factor equal to 1.39 for the case of diffuse reflection [41], P is the gas pressure, and ρ_d and r_d are the mass density and radius of the particles, respectively, k_B is the Boltzmann constant, M_g and T_g are the gas molecular mass and temperature, respectively.

The gas drag damping rate is listed for our experimental conditions in Tables II, III. It increases for heavier gas and for smaller particles. In the case of the highest damping rate (Xe, 4.8-μm particles) the damping length is $l = c/\nu_d = 4$ mm. The wave damping length is the distance from the cone axis to the wave where its amplitude decreases by a factor of e (natural logarithm exponent). Figure 7 shows that the wave propagates to at least that distance. This suggests that in the case of 4.8-μm particles gas drag is the limiting factor of the cone length. In the case of 8.9-μm particles the observed cone length is smaller, despite a lower damping rate. The latter result suggests that an additional mechanism is at work in limiting the length of the cones.

Another mechanism is dispersion. The supersonic disturbance launches a broad spectrum of Fourier components with different wave numbers. In the absence of damping, the wave energy propagates at the same acoustic speed for all long wavelengths, but not for short wavelengths. These short wavelengths will therefore gradually reduce the sharpness of a cone's wings, as the wave energy propagates outward.

Nonuniformities in the medium might also limit the size of the cone. For example, nonuniformities in the particle number density will lead to a nonuniform acoustic speed. Another possibility is nonuniformities in the plasma background, which can lead to a particle charge that varies spatially. There may be still other effects that we have not anticipated that will dissipate the cone as it propagates.

C. Charge

A particle immersed in a plasma acquires an electric charge by collecting ions and electrons from the gas phase. Here we will review methods of measuring charge used by previous experimenters, and then a method based on the Mach angle, which is the primary method we used in this paper.

The charge can be measured directly by laser-induced photodetachment in combination with a measurement of electron density using microwaves [44]. It can also be measured indirectly in several ways, including the observation of colliding particle trajectories [17,18].

Another indirect method of measuring the charge, which we used for two discharge conditions in this paper, is the vertical resonance method [24,45]. In the original method [24,45] the particles, while levitated in the sheath, are shaken by a low-frequency sinusoidal voltage applied as a modulation to the rf voltage on the lower electrode. The resonance frequency was determined and the particle charge calculated using the equation of motion, and the Poisson's equation, assuming that the sheath potential changes quadratically. Two limitations of this method are the assumption of a quadratic potential and the need for a value for the electron and ion densities at a location inside the sheath where it is impractical to insert the probe. One can measure the ion density at a location upstream from the sheath and then reduce this value by an arbitrary coefficient to estimate the density at the particle height. A second arbitrary coefficient, the ratio of the ion and electron densities, is also needed since these densities are not equal inside a sheath. In a variation on this method, one uses a measurement of the height of the particles rather than the ion density, thereby improving the accuracy of the input parameters [46]. Even so, one still has the limitation of assuming a quadratic sheath potential.

In this paper, our primary measurement was the method of Ref. [4]. Using the angle of a Mach cone in Eq. (1) yields the acoustic speed. Inserting this in a theoretical expression for the acoustic speed, which depends on charge, then yields a value for Q. For the theoretical expression we previously [4] used Eq. (6), which includes only the particle interactions with the six nearest neighbors. Here we improve on this by including second-nearest-neighbor interactions. The Debye length is a required input for this measurement, and this has the limitation that we are only able to measure λ_D upstream of the particle layer. Fortunately, it turns out that the particle charge is relatively insensitive to the uncertainty in a/λ_D, for the range of parameters in our experiment. The values we computed for the charge are presented in Tables IV and V. For comparison, we used the vertical resonance as an alternate method. For 8.9-μm particles in krypton of 50- and 100-W discharge, the vertical resonance frequency was 52 Hz, which corresponds to a charge of 38 000 and 33 000 electron charges, respectively. This is roughly twice the charge calculated from the measured Mach angle.

The particle charge is approximately the same for all discharge conditions. It depends most sensitively on the particle size. The latter result is expected in charging models [47], which predict that the particle's charge is proportional to its radius.

IX. CONCLUSION

Mach cones and shocks in a 2D Yukawa solid were studied experimentally using a strongly coupled complex plasma, i.e., a dusty plasma. The Mach cones were produced spontaneously by charged supersonic particles moving below the main crystal layer. The cones were found to have a double structure. In the first cone particles moved forward and in the

second they moved backward. The waves constituting the cone were shocks, where the first and second cones were analogous to the so-called loading and unloading waves in shocks in solids. Our imaging methods yielded measurements of the positions of individual particles. We devised methods of presenting the results as if the particles were a continuum, with a smooth number density and particle speed.

We tested the Mach angle relation, Eq. (1), and verified that it is accurate, at least over the limited range of Mach numbers accessible in our experiment. The acoustic velocity calculated for the second cone was 25% smaller than that for the first. The latter result might depend on nonlinear effects, i.e., upon the amplitude of disturbance created by the supersonic object.

Applying the Hugoniot relations to our results yielded a measure of the pressure increase behind the shock. This pressure increased by a factor of 1.3–1.6 so that the shock was classified as weak and thus close to an acoustic wave. The corresponding jump in the number density was a factor of 1.2–1.4. The shock was judged to be elastic because no defects were generated, except in a narrow track behind the supersonic particle.

As an empirical result that yields some information about the complex plasma in our experiment, we found that the acoustic velocity was the same within the experimental error for different discharge conditions, and that it was independent of particle size.

The charge of the particles in the crystal was calculated from the measurements of the Mach angle. This is a useful tool for complex plasma diagnostics.

The damping of the wave was explained by the gas drag for the smaller particles that we used. But there was an indication that other damping mechanisms were at work for bigger particles.

After the experiments in this paper were performed, another series of experiments [48] was carried out, producing Mach cones using a moving laser spot. The laser applied an optical pressure to the particles, and the spot was moved at a supersonic speed. This method allowed the experimenters to control the supersonic speed, rather than using Mach cones produced spontaneously by uncontrolled particles as in our experiment. The Mach cones created by the laser were generally similar to those excited by our charged particles, although there are some distinguishing features, as explained in detail in Ref. [48].

[1] R. Graham, *Solids Under High-Pressure Shock Compression* (Springer-Verlag, New York, 1993).

[2] O. Havnes, T. Aslaksen, T. Hartquist, F. Li, F. Melandsø, G. Morfill, and T. Nitter, J. Geophys. Res. [Space Phys.] **100**, 1731 (1995).

[3] O. Havnes, F. Li, F. Melandsø, T. Aslaksen, T. Hartquist, G. Morfill, T. Nitter, and V. Tsytovich, J. Vac. Sci. Technol. A **14**, 525 (1996).

[4] D. Samsonov, J. Goree, Z. W. Ma, A. Bhattacharjee, H. M. Thomas, and G. E. Morfill, Phys. Rev. Lett. **83**, 3649 (1999).

[5] J. Bond, K. Watson, and J. Welch, *Atomic Theory of Gas Dynamics* (Addison-Wesley, Reading, MA, 1965).

[6] N. Cheng, Z. Zhu, C. Cheng, and M. Toksöz, Geophysical Prospecting **42**, 303 (1994).

[7] F. J. Garcia de Abajo and P. Echenique, Phys. Rev. B **45**, 8771 (1992).

[8] F. J. Garcia de Abajo and P. Echenique, Phys. Rev. B **46**, 2663 (1992).

[9] F. J. Garcia de Abajo, video [online], available at ⟨http://electron.lbl.gov/~ccpgaabf/movies/wake_perp.html⟩.

[10] G. Crapper, *Introduction to Water Waves* (Harwood, Chichester, England, 1984).

[11] S. Hørluck and P. Dimon, Phys. Rev. E **60**, 671 (1999).

[12] H. Jaeger, S. Nagel, and R. Behringer, Rev. Mod. Phys. **68**, 1259 (1996).

[13] M. Hoppenbrouwers and W. van de Water, Phys. Rev. Lett. **80**, 3871 (1998).

[14] E. A. Allahyarov, L. I. Podloubny, P. P. J. M. Schram, and S. A. Trigger, Phys. Rev. E **55**, 592 (1997).

[15] H. M. Thomas and G. E. Morfill, J. Vac. Sci. Technol. A **14**, 501 (1996).

[16] J. Georges, G. Meille, J. Loubet, and A. Tolen, Nature (London) **320**, 342 (1986).

[17] U. Konopka, L. Ratke, and H. M. Thomas, Phys. Rev. Lett. **79**, 1269 (1997).

[18] U. Konopka, G. E. Morfill, and H. M. Thomas, in *Physics of Dusty Plasmas*, edited by Mihály Horányi and Scott Robertson, AIP Conf. Proc. No. **446** (AIP, College Park, MD, 1998), pp. 53–59.

[19] H. Ikezi, Phys. Fluids **29**(6), 1764 (1986).

[20] H. Thomas, G. Morfill, V. Demmel, J. Goree, B. Feuerbacher, and D. Möhlmann, Phys. Rev. Lett. **73**, 652 (1994).

[21] Y. Hayashi and K. Tachibana, Jpn. J. Appl. Phys., Part 2 **33**, L804 (1994).

[22] J. Chu and I. Lin, Physica A **205**, 183 (1994).

[23] J. Chu and I. Lin, Phys. Rev. Lett. **72**, 4009 (1994).

[24] A. Melzer, T. Trottenberg, and A. Piel, Phys. Lett. A **191**, 301 (1994).

[25] H. Thomas and G. Morfill, Nature (London) **379**, 806 (1996).

[26] A. Melzer, A. Homann, and A. Piel, Phys. Rev. E **53**, 2757 (1996).

[27] J. Pieper, J. Goree, and R. Quinn, Phys. Rev. E **54**, 5636 (1996).

[28] F. Melandsø, Phys. Plasmas **3**, 3890 (1996).

[29] A. Homann, A. Melzer, R. Madani, and A. Piel, Phys. Lett. A **173**, 242 (1998).

[30] M. Zuzic, H. Thomas, and G. Morfill, J. Vac. Sci. Technol. A **14**, 496 (1996).

[31] J. Pieper and J. Goree, Phys. Rev. Lett. **77**, 3137 (1996).

[32] X. Wang and A. Bhattacharjee, Phys. Plasmas **4**, 3759 (1997).

[33] M. Rosenberg and G. Kalman, Phys. Rev. E **56**, 7166 (1997).

[34] N. Rao, P. Shukla, and M. Yu, Planet. Space Sci. **38**, 543 (1990).

[35] P. Chaikin and T. Lubensky, *Principles of Condensed Matter Physics* (Cambridge University Press, New York, 1995).

[36] F. Peeters and X. Wu, Phys. Rev. A **35**, 3109 (1987).

[37] F. Chen, Plasma Phys. **7**, 47 (1965).

[38] V. Godyak and R. Piejak, Phys. Rev. Lett. **65**, 996 (1990).

[39] V. Godyak, R. Piejak, and B. Alexandrovich, Plasma Sources Sci. Technol. **1**, 36 (1992).

[40] R. Quinn, C. Cui, J. Goree, J. Pieper, H. Thomas, and G. Morfill, Phys. Rev. E **53**, R2049 (1996).

[41] P. Epstein, Phys. Rev. **23**, 710 (1924).

[42] M. J. Baines, I. P. Williams, and A. S. Asebiomo, Mon. Not. R. Astron. Soc. **130**, 63 (1965).

[43] L. Landau and E. Lifshitz, *Theory of Elasticity* (Pergamon Press, Oxford, 1970).

[44] E. Stoffels, W. W. Stoffels, G. M. W. Kroesen, and F. J. de Hoog, J. Vac. Sci. Technol. A **14**, 556 (1996).

[45] T. Trottenberg, A. Melzer, and A. Piel, Plasma Sources Sci. Technol. **4**, 450 (1995).

[46] J. Goree (unpublished).

[47] J. Goree, Plasma Sources Sci. Technol. **3**, 400 (1994).

[48] A. Melzer, S. Nunomura, D. Samsonov, and J. Goree (unpublished).